

Sonication-induced J-aggregation in nonhalogenated solvents boosts exciton delocalization for high-efficiency organic solar cells

Received: 17 June 2025

Accepted: 15 October 2025

Published online: 25 November 2025

Check for updates

Mingxu Zhou¹, Xinyue Xu², Dongrui Wang¹, Jiali Song³, Jiawei Qiao¹, Ruyue Zhang⁴, Yue Wu⁵, Tong Wang⁶, Jiwei Cui⁴, Christopher R. Hall², Hang Yin¹, Xiaoyan Du¹, Wei Qin¹, Kun Gao¹, Feng Chen¹, Zhixiang Wei⁶, Muthupandian Ashokkumar², Trevor A. Smith², Kangning Zhang¹✉, Yanming Sun³✉ & Xiaotao Hao^{1,2}✉

The commercialization of organic solar cells (OSCs) requires eliminating halogenated solvents. However, the disordered molecular aggregation of nonfullerene acceptors (NFAs) in nonhalogenated solvents hinders achieving high power conversion efficiencies (PCEs). Herein, this problem is addressed using an external physical field modulation strategy involving the sonication of NFA solutions to induce a transformation from disordered molecular aggregation to ordered J-aggregation via microstreaming and shear stress. The aggregation is effectively preserved within films, enhancing π - π stacking interactions. Moreover, sonication promotes the conversion of localized excitons to intra-moiety delocalized excitons and suppresses molecular vibrations. The PCEs of PM6:L8-BO-based binary and ternary devices fabricated using *o*-xylene are 19.43% and 20.41% (certified 19.84%), ranking among the highest values reported for nonhalogenated solvent-processed OSCs. The binary devices also exhibit high thermal stabilities (T_{80} lifetime > 10000 h). This universally applicable strategy effectively controls disordered aggregation in NFA solutions, thus paving the way for practical industrial applications.

Owing to their intrinsic flexibility, semitransparency, and remarkable cost-effectiveness, organic solar cells (OSCs) hold promise for next-generation photovoltaic technologies^{1–5}. Rapid advancements in material synthesis, molecular modification, and device engineering have resulted in single-junction OSCs with power conversion efficiencies (PCEs) exceeding 20%, which represents an important milestone on the road to industrial production^{6–10}. However, these PCEs are

strongly affected by spin-coating processes that rely on highly toxic halogenated solvents (such as chloroform) incompatible with large-scale production^{11–13}. In contrast, the low solubility of numerous nonfullerene acceptors (NFAs) in ecofriendly nonhalogenated solvents leads to substantial aggregation during processing^{14–17}, with disordered molecular orientations severely hindering exciton dissociation and charge transport. Consequently, a substantial efficiency gap

¹School of Physics, State Key Laboratory of Crystal Materials, Shandong University, Jinan, Shandong, P. R. China. ²School of Chemistry, The University of Melbourne, Parkville, Victoria, VIC, Australia. ³School of Chemistry, Beihang University, Beijing, P. R. China. ⁴Key Laboratory of Colloid and Interface Chemistry of the Ministry of Education, School of Chemistry and Chemical Engineering, Shandong University, Jinan, Shandong, China. ⁵College of Food Science and Technology, Nanjing Agricultural University, Nanjing, China. ⁶CAS Key Laboratory of Nanosystem and Hierarchical Fabrication, National Center for Nanoscience and Technology, Beijing, China. ✉e-mail: zhangkn@sdu.edu.cn; sunym@buaa.edu.cn; haoxt@sdu.edu.cn

exists between OSCs processed using halogenated and non-halogenated solvents^{18–21}, which highlights the importance of controlling NFA preaggregation in nonhalogenated solvents for achieving high photovoltaic performance^{22–25}.

The disordered aggregation state of NFAs in nonhalogenated solvents is typically transformed into more ordered H- or J-aggregation through deliberate induction to eliminate its adverse effects. Compared to H-aggregation (face-to-face stacking), J-aggregation is formed through intermolecular sliding packings, exhibiting distinctive photophysical properties in terms of expanding light absorption and enhancing charge transport²⁶. Various approaches have been explored to induce the formation of J-aggregation to improve the PCEs of OSCs. For example, Zhang et al. optimized the π - π stacking and refined the phase separation by promoting donor J-aggregation with highly volatile additives²⁶. Li et al. employed molecular modification to weaken the interaction between acceptor molecules and the solvent. This helps to facilitate pronounced J-aggregation, thereby enhancing charge extraction and inhibiting charge recombination²⁷. Despite the progress enabled by these approaches, the additive- and molecular-modification-based strategies involve complex synthesis and precise chemical control^{28,29}. These simplicity- and adaptability-related challenges hinder widespread practical applications of OSCs. External physical fields, such as heat, light, and electric stimuli, enable precise modulation of material solution state, film-formation process, and post-deposition metastable phases through straightforward processing^{30,31}. Ultrasound emerges as a uniquely powerful tool to selectively cleave noncovalent interaction networks via physical shear effects at the molecular scale by harnessing tunable acoustic cavitation energy^{32,33}. Concurrently, ultrasound-induced microstreaming can orchestrate molecular rearrangement, offering exceptional control over aggregation pathways. This efficient, ecofriendly approach that remains largely uncharted in organic photovoltaics holds significant potential to address the detrimental preaggregation of NFAs in nonhalogenated solvents. Elucidating the physical mechanism underlying the sonication-induced regulation of NFA aggregation is therefore essential for achieving high-performance OSCs processed by nonhalogenated solvents.

Herein, we use sonication to manipulate the preaggregation of NFAs in nonhalogenated solvents. The results of molecular dynamics simulations, quantum chemical computations, and multiple experiments demonstrate that sonication induces a transition from amorphous aggregation to ordered J-aggregation because of the effects of microstreaming and shear stress generated during the sonication process. Morphological studies reveal that sonication enhances intermolecular interactions in neat and blend films and thus promotes ordered molecular stacking. A global fitting model is developed to analyze transient absorption (TA) data to quantify the contributions of different charge separation (CS) pathways, and that of the pathways dominated by intra-moiety delocalized excitons is shown to markedly increase after sonication, which indicates a concomitant exciton dissociation enhancement. Sonication is also shown to inhibit molecular vibrations and thereby hinder nonradiative recombination. The binary and ternary OSCs prepared using sonication feature PCEs of 19.43 and 20.41% (certified 19.84%), respectively, along with high thermal stabilities (T_{80} lifetime > 10,000 h). The sonication strategy is applicable to other small-molecule and polymer acceptor systems, offering unique insights into the development of high-performance OSCs based on nonhalogenated solvents.

Results

Mechanism of sonication-regulated NFA aggregation

Figure 1a shows the chemical structures of the donor (PM6) and acceptor (L8-BO), and illustrates the sonication-assisted film fabrication processes based on the sequential deposition of these species. Initially, a PM6 layer is constructed on an indium tin oxide (ITO)

substrate, and a sonicated solution of L8-BO in *o*-xylene (*o*-XY) is deposited onto the PM6 layer. For numerous organic materials, amorphous aggregate formation due to nanoscale precipitation is observed in low-solubility solvents (such as *o*-XY), unlike in the case of high-solubility solvents (such as chloroform)³⁴. This problem is solved by using ultrasound filed. Sonication causes cavitation, i.e., the formation of tiny bubbles that can rapidly grow and collapse under the periodic pressure changes caused by ultrasonic waves³⁵ (Supplementary Fig. 1). The cavitation effect could alter molecular aggregation states via microstreaming and shear stress. We performed in-situ photoluminescence (PL) spectroscopy measurements of L8-BO solution (*o*-XY) to monitor the change in aggregation state during sonication (Fig. 1b and Supplementary Figs. 2–5). Combined with device data (which will be discussed subsequently), the optimal sonication condition was identified at 40 kHz, 720 W and 3 mins, as detailed in the Supplementary Information. However, sonication is typically accompanied by physical and chemical effects^{36,37}. In order to rule out the destructive on the material structure from chemical effects, we tested the Raman spectra of L8-BO solution before and after sonication, as shown in Supplementary Fig. 9. The unaltered peak positions after sonication suggest that no chemical reaction have occurred, but only physical effects exist.

Upon sonication, the emission peak of L8-BO shifted to substantially longer wavelengths, moving from 793 to 805 nm within three minutes (Fig. 1b), which indicated a concomitant increase in the extent of solution-phase J-aggregation³⁸. Notably, J-aggregation was well maintained in the solution within ten days after sonication was stopped (Supplementary Fig. 10), which was sufficient for spin-coating preparation of films and industrial production. Molecular dynamics simulations (see detail in Supplementary Information) were used to verify the effects of sonication on L8-BO molecules dissolved in *o*-XY (Fig. 1c). Without sonication (in the control system), the L8-BO molecules formed a dispersed state, with the radius of gyration (R_g) and solvent-accessible surface area (SASA) fluctuating around their mean values. Conversely, in the case of sonication, the R_g and SASA values notably decreased before stabilizing, suggesting that sonication increased the degree of aggregation (Fig. 1d and Supplementary Fig. 11). Root mean square deviations (RMSDs) were calculated to observe the overall conformational changes relative to the initial structure throughout the simulation period (Fig. 1e). In both systems, the RMSD initially increased before reaching equilibrium, which reflected rapid convergence toward a stable equilibrium state. The local magnification of simulation snapshots revealed that the control system contained some amorphous structures and H-aggregates, while a marked increase in the number of J-aggregates was observed after sonication, in line with the in-situ PL spectroscopy results.

Quantum chemical computations were performed to clarify the mechanisms underlying the sonication-induced J-aggregation (Supplementary Figs. 12a, b). An extended version of the Su-Schrieffer-Heeger tight-binding model was utilized, with a comprehensive description of the calculation process provided in the Supplementary Information³⁹. J-aggregation can be categorized into A-to-A and A-to-D types. Supplementary Fig. 12c shows the band gaps of different aggregation modes. The redshift of the PL spectrum is consistent with a reduction in band gap, suggesting a transformation into the A-to-D type J-aggregation. Hence, we focused exclusively on this type of J-aggregation in subsequent analyses. The results (Supplementary Figs. 12d, e) indicated that under various conditions, the aggregation energy of J-aggregation consistently exceeded that of H-aggregation, i.e., the latter aggregation was energetically preferred⁴⁰. Hence, NFAs tended to form H-aggregates in the absence of sonication. Cavitation bubbles are generated during the sonication process. As depicted in Supplementary Fig. 13, the periodic contraction and expansion of cavitation bubbles create a marked velocity gradient between the bubble surface and the surrounding solvent. This gradient

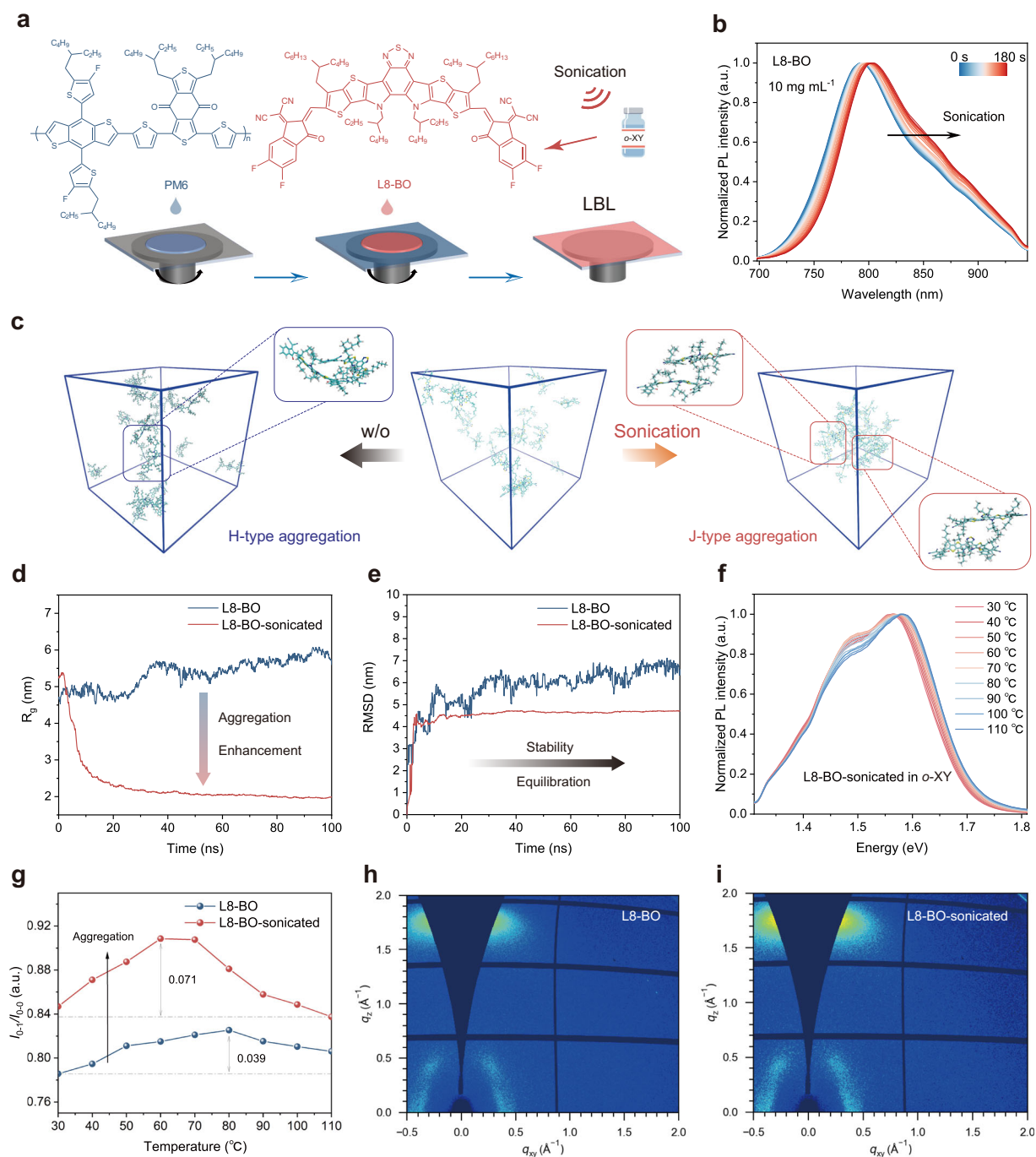


Fig. 1 | Mechanism underlying sonication effects probed by simulations, calculations and experiments. **a** Chemical structures of different materials and schematic of sonication-based processing. **b** Evolution of the photoluminescence (PL) spectra of the L8-BO solution during sonication (inset shows the PL changes at 1 min after stopping sonication). **c** Effects of sonication on the molecular dynamic behavior of L8-BO in *o*-XY. **d** Effects of sonication on the change in the radius of

gyration (R_g) with time. **e** Root mean square deviation–time plots obtained with and without sonication. **f** Temperature-dependent PL spectra of the sonicated L8-BO in *o*-XY. **g** Peak intensity ratio extracted from **(f)**. **h, i** Two-dimensional (2D) grazing-incidence wide-angle X-ray scattering (GIWAXS) patterns of the L8-BO films obtained without and with sonication. Source data are provided as a Source Data file.

drives the generation of microstreaming and shear stress (a pair of parallel reaction forces)⁴¹. Microstreaming pushes L8-BO molecules to aggregate on the bubble surface. Then the disordered molecules will be oriented and arranged under the effect of shear stress⁴², and subsequently become ordered J-aggregation. Meanwhile, the H-aggregation can overcome the energy barrier after acquiring energy and sliding to ordered J-aggregation.

The aggregation behavior of sonicated L8-BO in *o*-XY was investigated using temperature-dependent PL spectroscopy (Fig. 1f and

Supplementary Fig. 14). The long-wavelength shoulder peak (855 nm)/main peak (805 nm) intensity ratio ($I_{0.1}/I_{0.0}$) obtained through the double-peak fitting analysis of the PL spectra was employed to quantify the effects of sonication on the aggregation state at different temperatures (Fig. 1g and Supplementary Table 1)⁴³. Sonicated L8-BO exhibited more pronounced $I_{0.1}/I_{0.0}$ variations, along with a stronger dependence of this ratio on the solution temperature compared with the untreated sample, which manifested the enhanced intermolecular interactions and an increased tendency for aggregation. As mentioned

above, J-aggregation was well maintained in the solution phase, further influencing the film morphology. Subsequently, we analyzed the ultraviolet (UV)–visible absorption and PL spectra of the corresponding films (Supplementary Figs. 15 and 16). Sonication induced red shifts in the absorption and PL peaks of the L8-BO film, while predictably enhancing its crystallinity⁴⁴. This effect was quantitatively assessed using grazing-incidence wide-angle X-ray scattering (GIWAXS) measurements (Fig. 1h and i, Supplementary Fig. 17, and Supplementary Table 2). Prominent π – π stacking peaks of the control (1.753 Å) and sonicated (1.769 Å) L8-BO films were observed in the out-of-plane (OOP) direction⁴⁵. The decrease in d -spacing from 3.584 to 3.552 Å after sonication indicated a closer intermolecular packing. The calculated crystal coherence length (CCL) increased from 23.46 Å in the control film to 25.13 Å in the sonicated film. Thus, the sonicated L8-BO film exhibited a higher crystallinity and more ordered molecular stacking than its nonsonicated counterpart. Time-resolved photoluminescence (TRPL) measurements revealed that sonication increased the exciton lifetime of the L8-BO film from 471 to 641 ps, possibly by favoring ordered J-aggregation⁴⁶.

Blend film morphology

Sonicated L8-BO was combined with PM6 via sequential deposition to construct layer-by-layer (LBL)-type devices and thus assess the role of sonication in determining blend film morphology. According to the corresponding two-dimensional (2D) GIWAXS patterns (Fig. 2a, b), both PM6 and L8-BO exhibited a preferential face-on orientation in blend films, which favored charge transport, as evidenced by prominent (100) lamellar stacking peaks in the in-plane (IP) direction and strong (010) π – π stacking peaks in the OOP direction. After sonication, the CCL of the blend films increased from 24.48 to 27.32 Å, and the d -spacing decreased from 3.588 to 3.550 Å (Fig. 2c and Supplementary Table 3). These results suggested that sonication facilitated crystallization and ordered molecular stacking within the active layers. Grazing-incidence small-angle X-ray scattering (GISAXS) measurements were performed to characterize the donor and acceptor domain sizes in the blend films and thus investigate phase separation behavior at the nanoscale (Supplementary Fig. 12). The Debye–Anderson–Brumberger and fractal models were used for fitting⁴⁷. The relevant fitting steps are presented in the Supplementary Information, and the relevant fitting parameters are summarized in Supplementary Table 4, with ζ , η , D , and $2R_g$ representing the average correlation length of the PM6 phase, correlation length, fractal dimension of L8-BO clusters, and size of clustered L8-BO domains, respectively. After sonication, the $2R_g$ value of the blend films increased, indicating the expansion of acceptor-enriched domains, which facilitated the formation of an optimized morphology and suitable phase separation.

To further elucidate the potential mechanisms underlying the effect of sonication on active layer growth, we conducted in-situ UV–visible absorption spectroscopy to monitor the film-formation process of the PM6:L8-BO blends. The characteristic peaks of PM6 and L8-BO were observed within the ranges of 400–660 nm and 660–950 nm, respectively (Supplementary Fig. 19), and peak position changes were analyzed (Fig. 2d, e). Based on peak evolution, the film-formation process was divided into three stages: (i) solvent evaporation and crystal nucleation, (ii) crystallization, and (iii) film formation⁴⁸. Ordered aggregation in the sonicated L8-BO solution allowed the first stage to begin earlier, thus benefiting the prolonged molecular stacking in the second stage. The red shift of the L8-BO molecular peaks after the film-formation stage further corroborates the formation of J-aggregates. Additionally, during the film-formation process of L8-BO, the peak position of PM6 exhibited a notable blue shift, which was attributed to the immediate deposition of the L8-BO layer. The swelling effect resulted in the dissolution of a part of the donor layer during acceptor deposition, thus inducing additional mutual diffusion

between them. Importantly, the ordered J-aggregation of the L8-BO molecules markedly reduced the secondary film-formation time of the PM6 molecules, thus minimizing the diffusion from the acceptor layer into the donor layer and thereby hindering unnecessary mixing.

The effects of sonication on the surface morphology of thin films were probed by atomic force microscopy⁴⁹. Both the neat L8-BO and blend films exhibited increased root mean square (RMS) roughness values after sonication (Supplementary Fig. 20). The more refined fibrillar network structure in the blend films facilitated the formation of high-speed pathways for electron and hole transport. To distinguish donor and acceptor domains, the stretching of characteristic bonds was analyzed using photoinduced force microscopy (PiFM) (Supplementary Figs. 21–22, Fig. 2f, g). The line profiles extracted from the corresponding localized near-infrared images are presented in Fig. 2h, i. After sonication, the acceptor domains in the blend films exhibited fibrillar structures with an approximate diameter of 23 nm. The increase in the amount of small fibrillar structures indicated the formation of a fibrillar network between the donor and acceptor phases. The overlaid PiFM images of PM6 and L8-BO were used to further explore the sizes of the different phases (Supplementary Figs. 23)⁵⁰, revealing that sonication prevented excessive donor–acceptor mixing. This is beneficial for reducing geminate recombination and increasing the fill factor (FF), which will be discussed below.

Film-depth-dependent light absorption spectroscopy was conducted to analyze the effects of sonication on the vertical phase separation of the thin films (Supplementary Fig. 24)⁵¹. Sonication increased the acceptor concentration near the cathode, resulting in an optimized vertical gradient distribution within the blend films (Fig. 2j). This optimization was conducive to the rapid transfer of excitons to the acceptor phase after dissociation. The effects of sonication on the morphological evolution of the L8-BO molecular aggregates were rationalized as follows (Fig. 2k). Without sonication, the L8-BO molecules spontaneously formed H-type and amorphous aggregates in the solution. This disordered aggregation contributed to an irregular distribution within the solid film and adversely affected charge transfer (CT). Conversely, upon sonication, the L8-BO molecules formed ordered J-type aggregation in the solution. This preconstructed ordered aggregation was effectively retained during subsequent crystal growth stages, which promoted ordered molecular stacking and considerably enhanced π – π stacking interactions among molecules. Meanwhile, the sonication strategy optimized the phase separation of blend films and facilitated the formation of a fibrillar network. This sonication-induced morphological optimization can be expected to improve exciton and charge behaviors.

TA analysis of exciton delocalization

Femtosecond TA spectroscopy measurements were performed to probe the impact of the sonication-optimized microstructure on exciton and charge dynamics. The L8-BO acceptor was selectively excited at 800 nm. The 2D color maps of the TA spectra of the blend films produced from non- and sonicated solutions are presented in Fig. 3a and Supplementary Fig. 25a. The ground-state bleaching (GSB) signal of the PM6 donor at 580 nm was extracted and analyzed using exponential fitting to track hole transfer kinetics (Supplementary Fig. 26a and Supplementary Table 5)⁵². The decrease in lifetime of the sonicated films from 0.34 to 0.24 ps indicates a concomitant increase in the rate of hole transfer⁵³. The signal of the localized exciton (LE) state of the acceptor was extracted at 880 nm (Supplementary Fig. 26b). Sonication-induced morphology tuning considerably accelerated excited state decay (i.e., the lifetime decreased from 3.89 to 2.28 ps) and thus increased the efficiency of exciton dissociation (Supplementary Table 6)⁵⁴. In addition, the extended lifetime of the polaron signals observed at 960 nm revealed that bimolecular recombination was suppressed in the sonicated film³¹ (Supplementary Fig. 26c). Supplementary Fig. 26d showed the kinetic curves of the

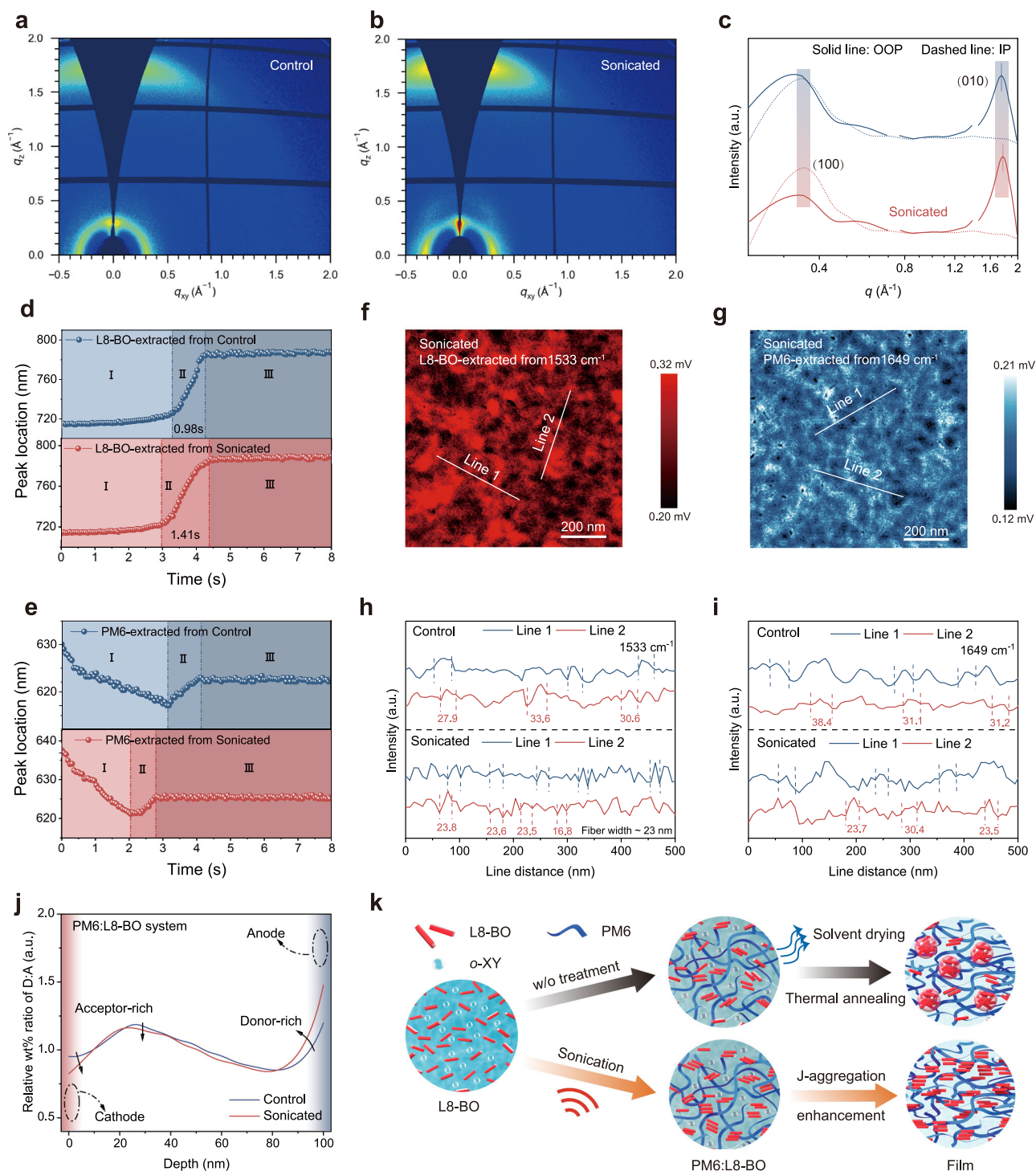


Fig. 2 | Morphological analysis of blend films. **a, b** 2D GIWAXS patterns of fresh PM6:L8-BO (*o*-XY) blend films obtained without and with sonication. **c** Out-of-plane and in-plane extracted line-cut profiles of the corresponding films. **d, e** UV-vis absorption peak locations of the acceptor and donor for the PM6:L8-BO films prepared without or with sonication. **f–i** Photoinduced force microscopy images acquired using wavenumbers of 1532 cm^{-1} (representing L8-BO) and 1648 cm^{-1}

(representing PM6) and line profiles recorded along the white arrows to obtain the fibril width for the PM6:L8-BO blend film prepared using sonication. **j** Film-depth-dependent composition profiles extracted from the depth-dependent light absorption spectra of blend films. **k** Schematic illustrating the regulation of film-formation process and crystallization kinetics for the PM6:L8-BO films prepared without or with sonication. Source data are provided as a Source Data file.

intra-moiety delocalized excitons (i-DE) extracted from TA spectra at 1500 nm^{55} . This signal was related to the exciton delocalization and will be discussed in detail below.

Global fitting was used to explore the effects of sonication on the contributions of different exciton dissociation pathways (Fig. 3b). The CS process is governed by competition between the LE \rightarrow i-DE \rightarrow CS and

LE \rightarrow CT \rightarrow CS pathways. The former pathway involves a rapid (within ~ 0.2 ps) transformation of LE states into i-DE states in the acceptor domain owing to strong intermolecular interactions among conjugated units. The i-DE states subsequently transform to CS states⁵⁵. The latter pathway resembles traditional models, with LE states diffusing to the donor/acceptor (D/A) interface, transforming to CT

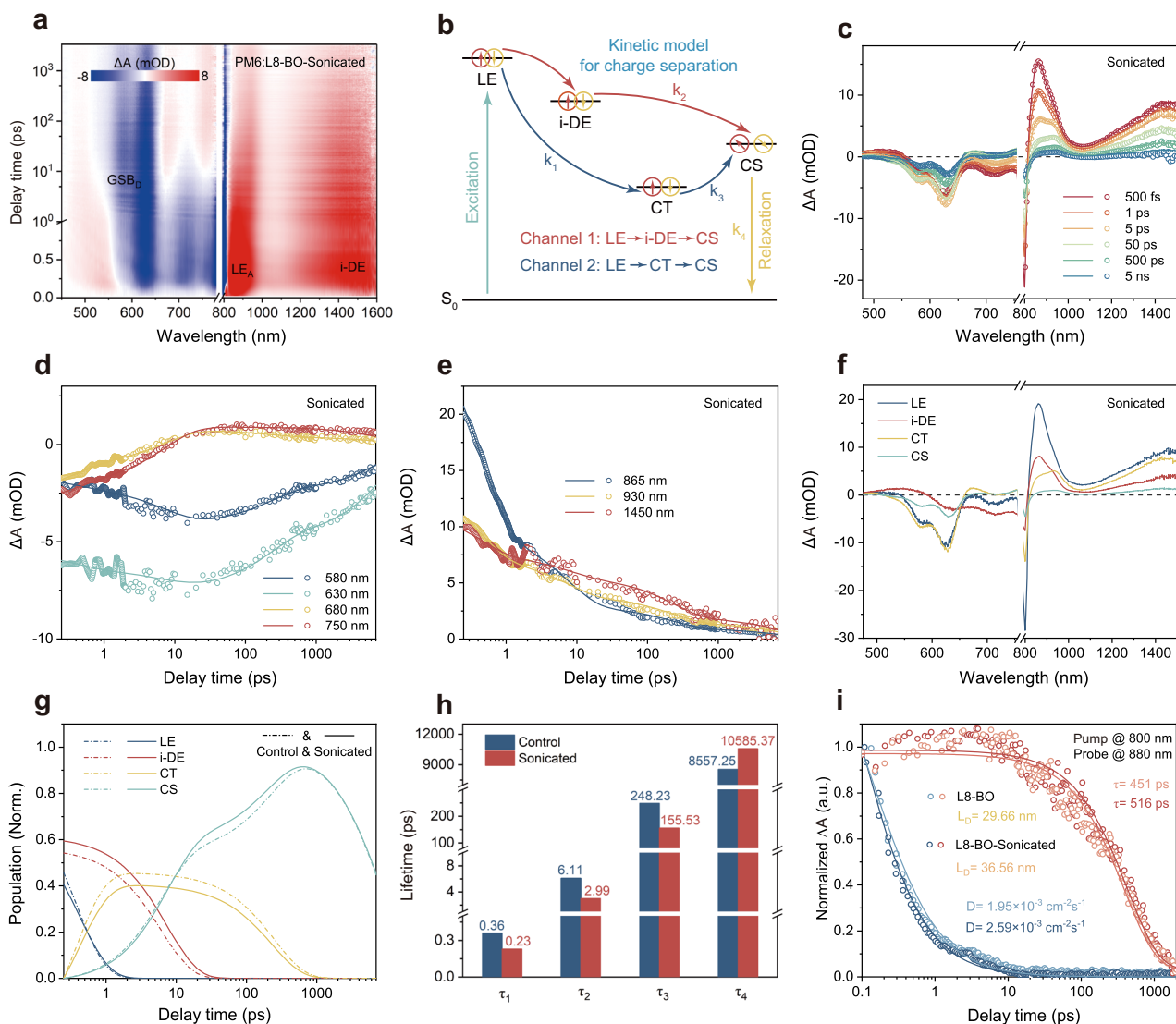


Fig. 3 | Global fitting analysis of exciton and charge dynamics. **a** Transient absorption (TA) spectral plot of the sample prepared using sonication. **b** Model used in TA global fitting. k , rate of evolution towards different states. **c** TA spectra with fitting curves obtained at different time delays for the sonicated sample. **d,e** TA dynamics and related fitting curves obtained for visible and infrared regions. **f,g** Localized exciton (LE), intra-moiety delocalized exciton (i-DE), charge transfer (CT), and charge separation (CS) signals extracted from TA spectra by global fitting,

along with the corresponding lifetime. **h** Lifetime of all signals in PM6:L8-BO films prepared without or with sonication. **i** Pump-fluence-dependent TA kinetics probed at 880 nm using L8-BO films prepared without or with sonication (The excitation intensity is 0.5 and 30 $\mu\text{J cm}^{-2}$, respectively). τ , exciton lifetime; D , exciton diffusion coefficient; L_D , exciton diffusion length. Source data are provided as a Source Data file.

states, and further dissociating into CS states. TA spectra recorded using different time delays were analyzed to extract the dynamic evolution signals corresponding to the LE, i-DE, CT, and CS states (Fig. 3c–f and Supplementary Figs. 25b–e), with the associated contributions shown in Fig. 3g. For both the control and the sonicated samples, the transient spectral features evolved on similar time scales. Under 1 ps, GSB features matching the steady-state absorption spectrum of the blend film were prominent in the visible region between 550 nm and 780 nm. A positive excited-state absorption (ESA) feature between 450 nm and 550 nm corresponding to the extracted spectrum of the i-DE state suggested the ultrafast formation of this state within the coherence time (~200 fs). This ESA returns to a negative GSB after tens of ps, indicating a progression of the system from the i-DE states to new intermediates (CT/CS). On the timescale of tens of hundreds of ps, whilst the GSB features were still present, the transient spectra adopt broad ESA features spanning from 650 to 1500 nm. This is similar to the CT/CS state ESA spectral features observed in PM6/Y6

systems⁵⁵. The spectrum of the CS state was similar to that of the CT state but with a more flattened ESA feature extending into the NIR region with an absence of a positive peak at ~660 nm. On a ~200 fs timescale, the sharp ESA of the LE state in the NIR region around 850 nm developed a more prominent shoulder around 960 nm, indicating the ultrafast formation of polarons upon formation of the CT state. The intensity of the NIR signal from 1000 to 1500 nm decayed much more slowly compared to the signal at 850–900 nm in the first 10 ps, and through global analysis, this signal was mainly attributed to the LE and the CT states.

After sonication, the contribution of the pathway dominated by i-DE states substantially increased (0.54 \rightarrow 0.6), which indicated that the resulting morphology in the sonicated films facilitate exciton delocalization. It can effectively reduce the dependence of exciton dissociation on the D/A interface^{55–57}. Figure 3h shows the fitted lifetime for each stage of the two pathways. The lifetime for all three stages after sonication ($\tau_1 = 0.23$ ps, $\tau_2 = 2.99$ ps, $\tau_3 = 156$ ps) were

notably shorter than those observed in the control system ($\tau_1 = 0.36$ ps, $\tau_2 = 6.11$ ps, $\tau_3 = 248$ ps). Accordingly, the rates of evolution towards successive states in the sonicated film ($k_1 = 4.35$ ps⁻¹, $k_2 = 0.33$ ps⁻¹, $k_3 = 0.0064$ ps⁻¹) were faster than that in the control film ($k_1 = 2.78$ ps⁻¹, $k_2 = 0.16$ ps⁻¹, $k_3 = 0.0040$ ps⁻¹). These results suggested that the sonication strategy promoted efficient exciton dissociation in both pathways. In addition, the lifetime of the CS state markedly increased after sonication (from 8.6 to 10.6 ns), which indicated suppressed charge recombination.

Exciton diffusion length (L_D) plays a crucial role in the CS pathway dominated by the CT state. To investigate the influence of sonication on L_D , we recorded the pump-fluence-dependent TA spectra of the L8-BO neat films (Supplementary Fig. 26e, f)⁵¹, revealing that the exciton decay rate increased with increasing excitation intensity. Two primary quenching pathways were considered, characterized by the intrinsic exciton decay rate coefficients (k) at any given excitation flux and bimolecular decay rate coefficients (γ) for exciton–exciton annihilation at high pump fluences⁵⁴. The following diffusion equation was used to globally fit the TA decay curves of the L8-BO acceptor:

$$\frac{dn(t)}{dt} = -kn(t) - \frac{1}{2}\gamma n^2(t) \quad (1)$$

Based on this equation, we derived a function describing the variation in singlet exciton density distribution n with time t :

$$n(t) = \frac{n(0)e^{-kt}}{1 + \frac{\gamma}{2k}n(0)[1 - e^{-kt}]} \quad (2)$$

where $\gamma = 8\pi RD$ (D is the exciton diffusion coefficient, and R is the annihilation radius of the singlet excitons (assumed to equal 1 nm)). The fitted parameters are listed in Supplementary Table 7. The exciton diffusion length ($L_D = \sqrt{D\tau}$) increased from 29.66 to 36.56 nm after sonication (Fig. 3i), indicating efficient exciton transport to the D/A interface and supporting the subsequent conversion to CT states. This agrees with the efficient CT suggested by the global fitting results, which is an essential prerequisite for achieving high-efficiency OSCs⁵⁸.

Molecular vibration and nonradiative recombination

Based on the aforementioned insights into exciton and charge dynamics, transient infrared (TRIR) spectroscopy was used to further examine the effects of the optimized morphology induced by sonication on molecular vibration (Fig. 4a, Supplementary Figs. 27a–c). We extracted the polaron dynamic curve within the 1700–1800 cm⁻¹ range, where the contributions from molecular vibrations were minimal (Fig. 4b). The blend films prepared using sonicated solutions demonstrated accelerated charge generation (i.e., the polaron signal rise time decreased from 9.17 to 6.64 ps) and slightly slowed charge recombination, in line with the TAS results. To analyze the transient vibrational spectra and dynamic changes precisely, we used a cubic polynomial function to fit the polaron background and deconvolute its contributions (Supplementary Fig. 28), as illustrated in Fig. 4c and Supplementary Fig. 27d⁵⁹. According to the FTIR spectra (Supplementary Fig. 21), the double-peak GSB absorption feature between 1500 and 1550 cm⁻¹ corresponds to L8-BO vibration (C=C bond in ring). These features were sharp at early times and broaden after 10 ps. The derivative-type feature with a positive peak at 1485 cm⁻¹ (-10 cm⁻¹ downshift from the main absorption peak) can most likely be attributed to hot ground states (S_0) or hot LE (with minimal structural distortion from the S_0).

This derivative signal decayed more rapidly in the sonicated sample (8.3 ps) compared to the control blend (10.7 ps, Fig. 4d) and was likely due to the faster heat dissipation in more structurally ordered molecular solids which allowed efficient propagation of phonons. Another noticeable difference was the vibrational peak

widths in the TRIR spectra. Figure 4e compares the GSB feature around 1533 cm⁻¹ at 850 ps for the control and the sonicated blend. The peak widths of the control were broader than the sonicated blend, hinting to the existence of a wider variety of relative molecular orientations, thus, a greater degree of disorder. Therefore, it was evident that the structural tuning via sonication successfully reduced the disorder in the film, allowing for efficient propagation of both thermal energy and charge. This result is further discussed with TRPL experimental results in a later section.

The removal of the polaron background allowed us to isolate the vibrational mode of PM6 at 1649 cm⁻¹ (see FTIR spectra in Supplementary Fig. 21a). The recovery of this GSB feature was faster in the sonicated blend (5.84 ps), whereas for the control blend (7.13 ps), a small ESA signal at 1670 cm⁻¹ slowly emerged after 10 s of ps. This subtle difference suggested that when CT/CS states formed, in the more structurally ordered sonicated film, the PM6 did not undergo much geometry change. However, in the control film, the PM6 was structurally disturbed in the CT/CS states, inducing a frequency shift. Another subtle difference was at 1750 cm⁻¹. In the control film, an ESA feature was observed after the pulse duration -300 fs and slowly recovered during the scan window. In the sonicated film, this ESA decayed into a clear bleach signal after several hundreds of ps. The FTIR of the sonicated L8-BO neat film compared to the untreated L8-BO hinted that this vibrational mode was likely associated with the presence of J-aggregated L8-BO (π - π stacked geometry). Given that the enhancement of this signal appeared at early times in both films, a possible explanation can be the formation of i-DE states within -200 fs enhanced neighboring L8-BO coupling through π - π stacking.

Temperature-dependent PL and TRPL spectra were recorded to further evaluate the effects of sonication on exciton–vibration coupling and thermally activated processes. With increasing temperature, the PL spectra shifted to shorter wavelengths and broadened (Supplementary Fig. 29). The interactions between excitons and molecular vibrations can be inferred from the peak positions⁶⁰, which are quantitatively described by:

$$E(T) = E(0) - \frac{2\alpha}{\exp(\theta/T) - 1} \quad (3)$$

where $E(0)$ is the bandgap energy at absolute zero (0 K), α is the intensity of the exciton–vibration interaction, and θ is the average phonon temperature. The sonicated films demonstrated reduced α from 151.2 to 113.3 meV (Fig. 4g and Supplementary Table 8) and was therefore concluded to inhibit exciton–vibration coupling and promote exciton diffusion and polaron transport. By fitting a series of temperature-dependent TRPL spectra (Supplementary Fig. 30), we obtained the temperature dependence of the nonradiative recombination rate, K_{nr} (Fig. 4h). In high-temperature regions, K_{nr} was more sensitive to temperature changes than in low-temperature regions because of the increase in molecular vibrations induced by thermal energy⁶¹. Moreover, a thermally activated process occurred between the S_0 and excited states (S_1)⁶² (Fig. 4i). Molecular vibrations led to the formation of an overlapping surface between S_0 and S_1 , which introduced an additional pathway for internal conversion processes⁶³. As discussed previously, sonication-induced structural tuning with ordered J-aggregate geometry allows for rapid thermal energy redistribution and dissipation⁶¹, which deactivates the thermally-activated non-radiative recombination of excitons.

Photovoltaic characteristics

To substantiate the benefits of the ordered J-aggregation induced by sonication, we fabricated LBL-type OSCs with an ITO/PEDOT:PSS/active layer/PDINN/Ag structure and tested the device performance under different sonication frequencies, power and duration (Supplementary Figs. 31–33 and Supplementary Tables 9–15). Details on the

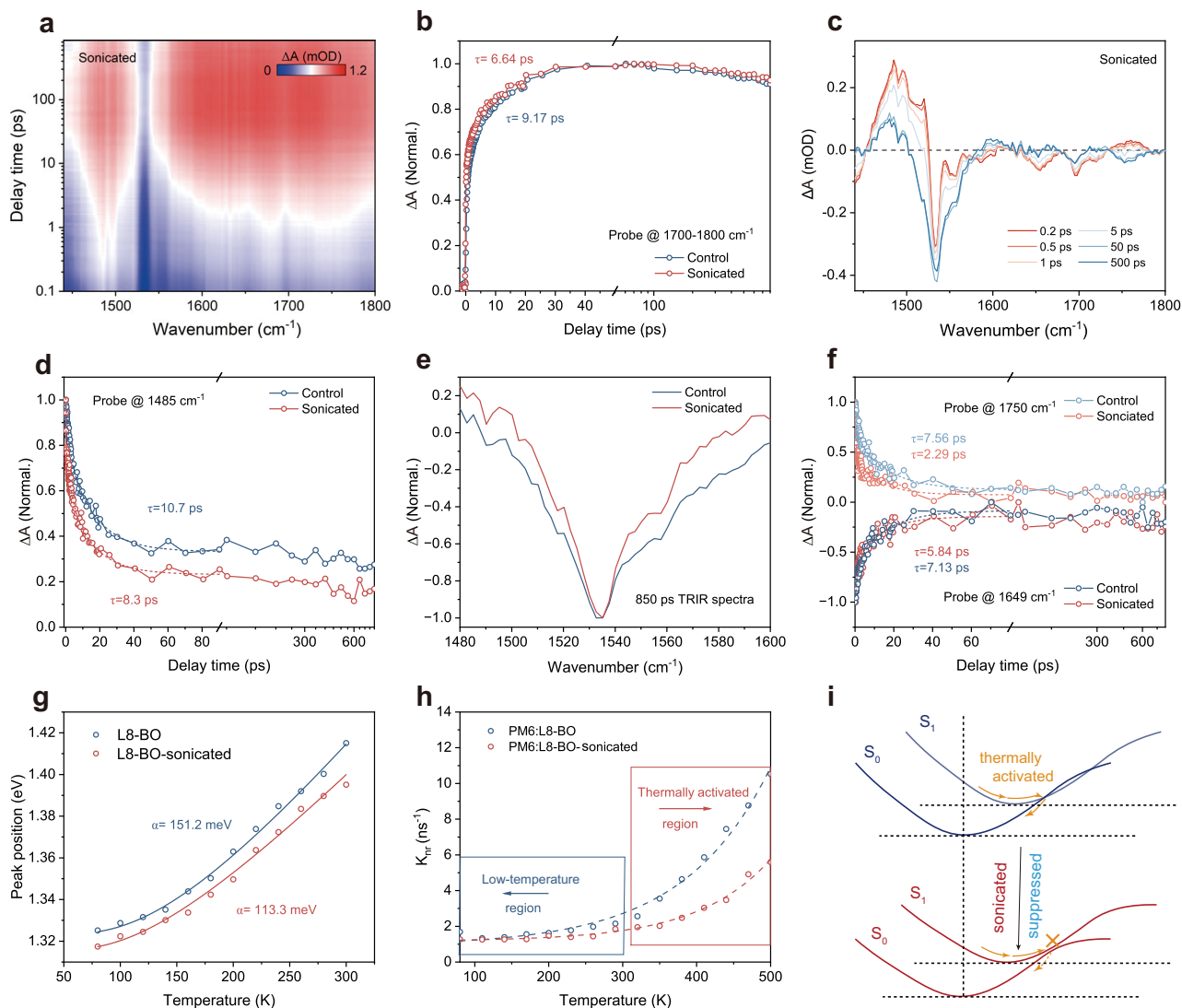


Fig. 4 | Excited-state dynamics revealed by transient infrared (TRIR) spectroscopy. **a** 2D color plots of TRIR data for the PM6:L8-BO films prepared using sonication. **b** TRIR spectra obtained after deconvoluting the signals of polarons for the PM6:L8-BO films prepared using sonication. τ , decay time. **c** TRIR profiles recorded at 1700–1800 cm^{-1} . **d** TRIR profiles obtained at 1485 cm^{-1} . τ , decay time. **e** TRIR spectra extracted from 850 ps. **f** TRIR profiles obtained at 1649 and 1750 cm^{-1} .

g Gaussian-fitted peak position as a function of temperature in L8-BO films prepared without or with sonication. α , intensity of the exciton-vibration interaction. **h** Nonradiative recombination rate as a function of temperature in the PM6:L8-BO films prepared without or with sonication. **i** Schematic of sonication modulating the thermally activated process between the ground (S_0) and excited states (S_1). Source data are provided as a Source Data file.

preparation and optimization are provided in the Supplementary Information. The J - V curves and photovoltaic parameters of the optimized devices are presented in Fig. 5a and Table 1. The control device achieved a PCE of 17.50%, an open-circuit voltage (V_{OC}) of 0.878 V, a short-circuit current (J_{SC}) of 25.36 mA cm^{-2} , and a FF of 78.56%, in agreement with previously published results^{64,65}. By controlling the sonication condition, we achieved a notably increased PCE of 19.43%, a V_{OC} of 0.881 V, a J_{SC} of 27.05 mA cm^{-2} , and a FF of 81.53%. Compared with that of the control, the external quantum efficiency (EQE) spectrum of the sonication-processed device was shifted to longer wavelengths. Similar to internal quantum efficiency (IQE), it also exhibited a higher full-spectrum response (Fig. 5b and Supplementary Fig. 34), as evidenced by more efficient exciton dissociation and charge extraction (Supplementary Fig. 35 and Supplementary Table 20). Subsequently, we fabricated ternary PM6:D18:L8-BO devices with different active layer thicknesses. The device with a 100 nm-thick active layer featured an increased PCE of 20.41% (certified as 19.84% by the National Institute of Metrology, China) (Fig. 5c and Supplementary

Fig. 36), a V_{OC} of 0.899 V, a J_{SC} of 27.43 mA cm^{-2} , and a FF of 81.19%; this PCE is one of the highest values reported for OSCs prepared using nonhalogenated solvents (Fig. 5d, Supplementary Tables 21 and 22). The 300 nm-thick device demonstrated a satisfactory PCE of 18.29%, with the FF (76.19%) ranking among the top values reported for an active layer thickness of 300 nm. The corresponding EQE spectra are presented in Supplementary Fig. 37. All J_{SC} values extracted from the J - V curves differed from the integrated current density of the EQE by <5%, thereby confirming the reliability of the photovoltaic performance.

To explore the potential of the sonication strategy for scalable industrial application, we fabricated flexible devices (1 cm^2) using the roll-to-roll technique in air. The devices were fabricated using an inverted structure of PET/Ag-grid/PH1000/ZnO/active layer/MoO_x/Ag. The detailed fabrication process is presented in the Supplementary Information. The J - V curves and device parameters are shown in Supplementary Fig. 38 and Supplementary Table 23. The control devices exhibited a PCE of 12.06%, a V_{OC} of 0.826 V, a J_{SC} of 21.71 mA cm^{-2} , and a

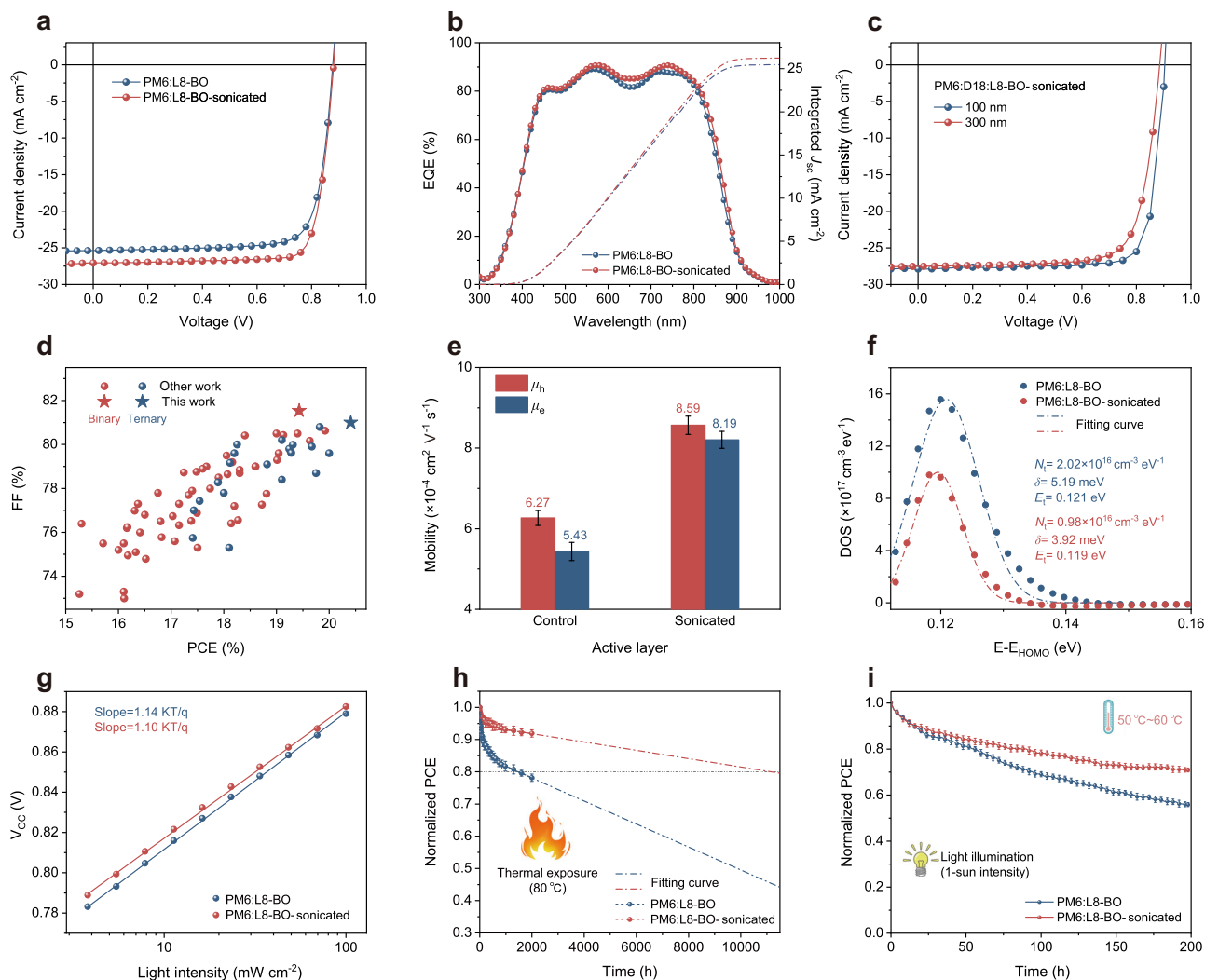


Fig. 5 | Photovoltaic properties of organic solar cells. a, b J - V curves and external quantum efficiency spectra of the devices prepared without or with sonication. **c** J - V curves of the devices with ternary active layers of different thickness prepared using sonication. **d** Positions of different binary and ternary systems in the FF-PCE space relative to those of previously reported systems. **e** Carrier mobilities of the control and sonication-processed devices obtained using space charge limited current (SCLC) measurements. **f** Density of trap states of the blend films and corresponding Gaussian fitting results. N_t , total density; δ , disorder parameter; E_t , center of DOS. **g** Measurements of light-intensity-dependent V_{OC} under different conditions. **h, i** Normalized PCEs obtained for the PM6:L8-BO devices prepared without or with sonication during thermal stability evaluation at 80 °C and photothermal stability evaluation under continuous illumination (100 mW cm⁻², white light-emitting diode) at 50 °C–60 °C. Error bars, centered on the mean, represent standard deviation for ten independent devices. Source data are provided as a Source Data file.

FF of 67.28%. After sonication, the device performance was improved, with a PCE of 14.04%, a V_{OC} of 0.828 V, a J_{SC} of 23.89 mA cm⁻², and a FF of 71.00%. The corresponding EQE spectra are shown in Supplementary Fig. 38b, with the integration current error controlled within 5%. The significant improvement in device performance indicates that the sonication strategy is also effective for devices prepared by the roll-to-roll technique, which holds critical implication for their industrial production.

The space charge limited current method was used to evaluate the charge transport which is related to the FF between the devices prepared under control and sonication conditions (Supplementary Fig. 39). The calculated hole and electron mobilities are presented in Fig. 5e and Supplementary Table 24. Sonication increased hole mobility (μ_h) from 6.27×10^{-4} cm² V⁻¹ s⁻¹ to 8.59×10^{-4} cm² V⁻¹ s⁻¹ and electron mobility (μ_e) from 5.43×10^{-4} cm² V⁻¹ s⁻¹ to 8.19×10^{-4} cm² V⁻¹ s⁻¹. The higher mobility and lower μ_h/μ_e ratio observed for the devices prepared under sonication conditions indicated more efficient and balanced charge transport⁴⁵. The density of trap states (N_t) was

calculated using frequency-dependent capacitance spectra recorded under dark conditions (Fig. 5f). The decrease in N_t from 2.02×10^{16} cm⁻³ eV⁻¹ to 0.98×10^{16} cm⁻³ eV⁻¹ indicated that sonication effectively prevented trap state generation⁶⁶. The relationship between J_{SC} and light intensity (P_{light}) was fitted as $J_{SC} = (P_{light})^\alpha$ (Supplementary Fig. 40a). Sonication increased α from 0.988 to 0.994 and thus effectively inhibited bimolecular recombination processes⁵⁷. The lower slope of the $V_{OC} - \ln(P_{light})$ plot observed for the sonicated film (Fig. 5g) signified the suppression of trap-assisted recombination, thereby enhancing charge transport in the OSCs⁶⁸. The increase in carrier lifetime from 5.83 to 7.44 μ s revealed by transient photovoltage (TPV) tests supported this observation (Supplementary Figs. 40b–c). Transient photocurrent (TPC) tests revealed accelerated charge extraction (i.e., fitting lifetime decreased from 0.35 to 0.26 μ s) in the devices prepared under sonication conditions. Energy loss was evaluated based on the measurements of the electroluminescence (EL) spectra, the external quantum efficiency of electroluminescence (EQE_{EL}), and the sensitive external quantum efficiency (sEQE) measured by Fourier transform

Table 1 | Photovoltaic parameters of PM6:L8-BO-based OSCs (prepared under different conditions using o-XY) under AM 1.5 G/100 mW cm⁻² illumination

Active layer	J_{SC} (mA cm ⁻²)	J_{SC}^{Cal} (mA cm ⁻²)	V_{OC} (V)	FF (%)	PCE ^a (%)
PM6:L8-BO	25.36	24.98	0.878	78.56	17.50 (17.28 ± 0.19)
PM6:L8-BO-sonicated	27.05	26.24	0.881	81.53	19.43 (19.22 ± 0.16)
PM6:D18:L8-BO-sonicated	27.88	26.55	0.904	81.00	20.41 (20.28 ± 0.12)
PM6:D18:L8-BO-sonicated	27.54 ^b	–	0.889 ^b	81.04 ^b	19.84 ^b
PM6:D18:L8-BO-sonicated-300 nm	27.51	26.64	0.885	76.19	18.29 (18.12 ± 0.11)

^{Cal}Integrated J_{SC} values obtained using external quantum efficiency measurements.

^aAverage PCEs with standard deviations determined using ten individual devices.

^bCertified by the National Institute of Metrology, China.

photocurrent spectroscopy (FTPS-EQE) (Supplementary Fig. 41 and Supplementary Table. 26). It was concluded that sonication slightly suppressed the energy loss, especially non-radiative recombination loss ΔE_3 (from 0.243 to 0.239 eV). Meanwhile, the extracted Urbach energy decreased from 24.16 to 23.57 meV, suggesting a concomitant reduction in energy disorder⁶⁹, which is aligned with the decrease of radiative recombination loss ΔE_2 (from 0.076 eV to 0.074 eV). These results confirm that sonication can be used to improve OSC performance.

Given that sonication can improve OSC efficiency, one can reasonably anticipate that it may also increase device stability. To minimize the adverse impact of organic interfacial layers on stability, we fabricated inverted devices with an ITO/ZnO/active layer/MoO₃/Ag configuration. Thermal stability was assessed upon continuous annealing in dry nitrogen atmosphere at 80 °C (Fig. 5h). Compared with the control devices, the sonication-processed devices (ten independent cells) exhibited a markedly reduced burn-in loss and an improved thermal stability. PCE decay was subjected to linear fitting, and the results indicated that the T_{80} lifetime of the optimized devices markedly exceeded 10000 h. We also tested the photothermal stability of OSCs under continuous illumination at 100 mW cm⁻² (50 °C–60 °C), revealing that sonication also increased resistance to photothermal stress (Fig. 5i).

To elucidate the mechanism by which sonication improved morphological stability, we extracted the normalized photovoltaic parameters (V_{OC} , J_{SC} and FF) over aging time for PM6:L8-BO-based devices, as shown in Supplementary Fig. 42. The control devices remained relatively stable V_{OC} and J_{SC} , whereas FF showed a marked decline. In contrast, the sonicated devices exhibited robust FF, indicating that sonication could suppress the degradation in mixed amorphous regions^{70,71}. Additionally, the sonicated films showed slight attenuation of CCL values (from 27.32 to 26.93 Å) after continuous thermal aging for 200 h compared to that (from 24.48 to 23.08 Å) of controls (Supplementary Fig. 43 and Supplementary Table. 27), suggesting the better stability in crystalline regions. Further thermodynamic analysis was conducted on neat L8-BO films and PM6:L8-BO blend films through the glass transition temperature (T_g) measurements (Supplementary Figs. 44 and 45). The sonicated samples displayed higher T_g than the controls, indicating that sonication reduced the diffusion coefficient of material in mixed amorphous region and enhanced the kinetic stabilization of film morphology^{9,72}. The results demonstrate the advantages of the sonication-improved active layer morphology for improving device stability.

Application scope of the sonication strategy

To explore the application scope of the ultrasound-field-based regulation of ordered J-aggregation in NFAs, we recorded the in-situ PL spectra of other PM6:NFA systems, including BTP-eC9, PY-IT, and PY-DT, during the sonication process (Fig. 6a–c). In addition to the continuous red shift of the PL spectra, we observed the continuous

intensification of the long-wavelength shoulder peaks of the PY-IT and PY-DT polymer acceptors, which suggested a concomitant increase in the extent of J-aggregation. We also recorded the temperature-dependent PL spectra of these systems (Supplementary Fig. 47) and extracted the corresponding I_{0-1}/I_{0-0} peak intensity ratios (Fig. 6d–f and Supplementary Table 28). The results showed enhanced temperature dependence, indicating intermolecular interaction and aggregation enhancement. Subsequently, solar cells based on these three systems were fabricated using a conventional device structure (Supplementary Fig. 48). The corresponding J – V curves are shown in Fig. 6g–i, and the device parameters are summarized in Supplementary Table 29. The sonication-processed PM6:BTP-eC9, PM6:PY-IT, and PM6:PY-DT devices achieved improved PCEs of 19.31, 18.32, and 18.71% compared to control systems, respectively. These results demonstrate the broad application scope of the sonication strategy.

Discussion

The NFA aggregation state in a nonhalogenated solvent was modulated using sonication. The combined results of simulations, computations, and experiments demonstrate that sonication induced the formation of ordered J-aggregates within the NFA solutions and films through microstreaming and shear stress. Morphological characterizations revealed that sonication improved phase separation during film formation, enhancing π – π stacking interactions and optimizing the molecular arrangement. The global fitting of TA data indicated that sonication increased the proportion of CS pathways dominated by i-DE states, thereby enhancing exciton dissociation. TRIR data showed the structural tuning effect on heat and carrier transport in the system, and together with temperature-dependent TRPL data further validated the inhibitory effect of sonication on nonradiative recombination. The PM6:L8-BO devices exhibited a high PCE of 19.43% and superior thermal stability (T_{80} lifetime > 10000 h). The addition of D18 to the PM6:L8-BO system resulted in a remarkable PCE of 20.41% (certified PCE of 19.84%), which is among the highest efficiencies reported for OSCs prepared using nonhalogenated solvents. The developed sonication strategy was demonstrated to have a broad application scope, as exemplified by its applicability to small-molecule and polymer acceptor systems. Thus, our work provides a practical approach to the fabrication of efficient, stable, and ecofriendly OSCs, facilitating their large-scale industrial production.

Methods

Measurements of PL and TRPL spectra

The PL spectra and TRPL experiments were performed using a confocal optical microscope, specifically the Nanofinder FLEX2 from Tokyo Instruments, Inc. This setup was equipped with a time-correlated single-photon counting (TCSPC) module, the Becker & Hickl SPC-150. For all PL spectrum measurements, a charge-coupled device (CCD) sensor, model DU420A-OE from Andor, was utilized. The excitation wavelength was consistently set at 400 nm, and the

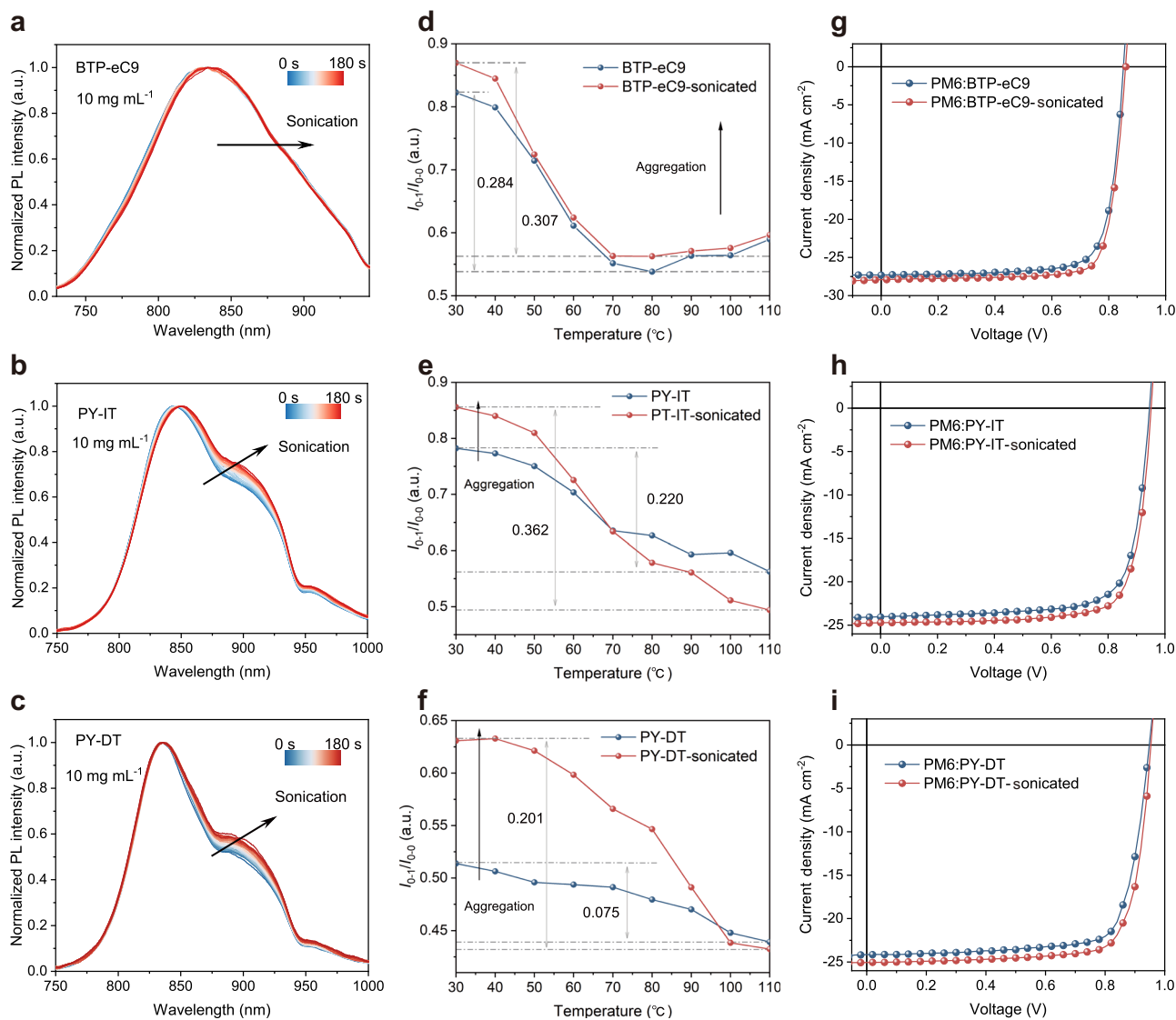


Fig. 6 | Photovoltaic characterization of other sonicated systems. a–c Evolution of the PL spectra of BTP-eC9, PY-IT and PY-DT solutions during sonication, with inset illustrating the changes in PL spectra at 1 min post sonication. **d–f** Peak ratios

extracted from the temperature-dependent PL spectra of BTP-eC9, PY-IT and PY-DT prepared without or with sonication. **g–i** V - J curves of different systems prepared without or with sonication.

excitation power for both PL spectra and TRPL experiments was maintained at 1 μ W. The laser spot had an approximate diameter of 8 μ m, resulting in an area calculated as $S = 5.02 \times 10^{-7}$ cm².

Measurements of AFM and PiFM Images

AFM measurements were performed on a Bioscope Resolve AFM (Bruker) in a tapping mode under ambient conditions. Photo-induced Force Microscopy (PiFM) measurements were performed by employing Anfattec Instruments AG (Oelsnitz, Germany).

Measurement of TA spectra

Femtosecond TA spectra were recorded using an optical setup that incorporated a Ti:sapphire femtosecond laser (from Coherent) in conjunction with an optical parametric amplifier (OPA) system. The 800 nm pulse emitted by the laser was divided into two beams via a beam splitter. One of these beams was directed into the optical parametric amplifier (TOPAS, Coherent) to generate pump pulses at 600 nm. The second beam was focused onto both sapphire and YAG plates to produce a white light supercontinuum, which served as the probe beams with a spectral range of 750–1600 nm. The initial pulses

were also split into two paths; one path led to the OPA for generating 400 and 750 nm pump pulses utilized in this study, while the other path produced a broad spectrum of probe light spanning from 520–800 nm (visible) and from 850–1300 nm (NIR).

Measurement of TRIR spectra

TRIR spectra were acquired using pump and probe beams generated through nonlinear optical processes utilizing the 1030 nm fundamental output from a Ytterbium-based laser oscillator (Pharos, Light Conversion). An optical parametric amplifier (OPA, Orpheus, Light Conversion), in conjunction with difference frequency generation (DFG, Lyra, Light Conversion), produced pump pulses with highly tunable wavelengths across the UV–NIR spectrum (210–2660 nm, ~150 fs temporal FWHM, ~5 nm bandwidth), operating at a base repetition rate of 100 kHz. The laser output was pulse picked to 10 kHz and a mechanical chopper (Thorlabs, MCIF60) was employed to reduce the pump repetition rate to 5 kHz while maintaining a probe rate of 10 kHz. The pump beam traversed a mechanical delay stage (Newport ESP300) to achieve optical delay times ranging from -50 to 900 ps and was subsequently focused to attain an approximate spatial diameter of

FWHM ~ 420 μm at the sample location. Linear polarization devices were utilized to control the relative polarization between the pump and probe beams at the magic angle. The mid-infrared probe spanning wavelengths from 4000 to 13000 nm with a temporal FWHM of less than 180 fs, was generated by an OPA and DFG system (ORPHEUS TWINS, Light Conversion). Given that atmospheric moisture and particulate matter significantly absorb mid-infrared radiation, all components of the probe pathway were enclosed under nitrogen within sealed boxes and conduits. TRIR spectra were captured using a polychromator-based IR spectrometer cooled with liquid nitrogen during experiments (Horiba iHR320 integrated with an FPAS 128-element MCT detector; Infrared Systems; spectral acquisition rate: 10 kHz; bandwidth: $\sim 300\text{ cm}^{-1}$). The sample was affixed to an X-Z translation stage controlled by two stepper motors for raster scanning purposes.

Reporting summary

Further information on research design is available in the Nature Portfolio Reporting Summary linked to this article.

Data availability

The data that support the findings of this study are available within the article and its Supplementary Information/Source Data file. Source data are provided with this paper.

References

1. Luo, S. et al. Auxiliary sequential deposition enables 19%-efficiency organic solar cells processed from halogen-free solvents. *Nat. Commun.* **14**, 6964 (2023).
2. Ma, L. et al. Design of low-cost non-fused ultranarrow-band-gap acceptors for versatile photovoltaic applications. *Joule* **8**, 2238–2249 (2024).
3. Chen, Z. et al. Local dipole modulation toward high fill factor in organic solar cells. *Adv. Mater.* **8**, 2408858 (2024).
4. Wang, Y. et al. Origins of the open-circuit voltage in ternary organic solar cells and design rules for minimized voltage losses. *Nat. Energy* **8**, 978–988 (2023).
5. Ding, P. et al. U-shaped dimeric acceptors for balancing efficiency and stability in organic solar cells. *Adv. Mater.* **42**, 2414080 (2024).
6. Wang, S. et al. Achieving 20% efficiency in organic solar cells through conformationally locked solid additives. *Adv. Energy Mater.* **25**, 2405205 (2024).
7. Zou, W. et al. Extending exciton diffusion length via an organic-metal platinum complex additive for high-performance thick-film organic solar cells. *Adv. Mater.* **37**, 2413125 (2024).
8. Wang, J. et al. Isomerism effect of 3D dimeric acceptors for non-halogenated solvent-processed organic solar cells with 20% efficiency. *Angew. Chem. Int. Ed.* **64**, e202423562 (2024).
9. Chen, C. et al. Molecular interaction induced dual fibrils towards organic solar cells with certified efficiency over 20%. *Nat. Commun.* **15**, 6865 (2024).
10. Kong, X. et al. Suppressed non-radiative loss and efficient hole transfer at a small highest occupied molecular orbital offset endows binary organic solar cells with 19.73% efficiency and a small efficiency-cost gap. *Energy Environ. Sci.* **18**, 386–396 (2025).
11. Lang, Y. et al. Balanced miscibility and crystallinity by 2D acceptors enabled halogen-free solvent-processed organic solar cells to achieve 19.28% efficiency. *Adv. Mater.* **37**, 2413270 (2025).
12. Zhang, Y. et al. Graded bulk-heterojunction enables 17% binary organic solar cells via nonhalogenated open air coating. *Nat. Commun.* **12**, 4815 (2021).
13. Chen, H. et al. Heterogeneous nucleating agent for high-boiling-point nonhalogenated solvent-processed organic solar cells and modules. *Adv. Mater.* **16**, 2404571 (2024).
14. Fan, B. et al. Enabling high efficiency of hydrocarbon-solvent processed organic solar cells through balanced charge generation and non-radiative loss. *Adv. Energy Mater.* **11**, 2101768 (2021).
15. Fan, B. et al. Optimisation of processing solvent and molecular weight for the production of green-solvent-processed all-polymer solar cells with a power conversion efficiency over 9%. *Energy Environ. Sci.* **10**, 1243–1251 (2017).
16. Zhao, H. et al. Hot hydrocarbon-solvent slot-die coating enables high-efficiency organic solar cells with temperature-dependent aggregation behavior. *Adv. Mater.* **32**, 2002302 (2020).
17. Wu, X. et al. Introducing a phenyl end group in the inner side chains of A-DA'D-A acceptors enables high-efficiency organic solar cells processed with nonhalogenated solvent. *Adv. Mater.* **35**, 2302946 (2023).
18. Xu, X. et al. Highly efficient non-fullerene organic solar cells enabled by a delayed processing method using a non-halogenated solvent. *Energy Environ. Sci.* **13**, 4381–4388 (2020).
19. Fan, B. et al. Importance of structural hinderance in performance–stability equilibrium of organic photovoltaics. *Nat. Commun.* **13**, 5946 (2022).
20. Zhao, W. et al. Vacuum-assisted annealing method for high efficiency printable large-area polymer solar cell modules. *J. Mater. Chem. C* **7**, 3206–3211 (2019).
21. Zhao, W. et al. Environmentally friendly solvent-processed organic solar cells that are highly efficient and adaptable for the blade-coating method. *Adv. Mater.* **30**, 1704837 (2018).
22. Li, H. et al. Advances in the device design and printing technology for eco-friendly organic photovoltaics. *Energy Environ. Sci.* **16**, 76–88 (2023).
23. Chen, H. et al. 17.1%-efficient eco-compatible organic solar cells from a dissymmetric 3D network acceptor. *Angew. Chem. Int. Ed.* **60**, 3238–3246 (2021).
24. Zhuo, H. et al. Giant molecule acceptor enables highly efficient organic solar cells processed using non-halogenated solvent. *Angew. Chem. Int. Ed.* **62**, e202303551 (2023).
25. Pröller, S. et al. Following the morphology formation in situ in printed active layers for organic solar cells. *Adv. Energy Mater.* **6**, 1501580 (2016).
26. Song, J. et al. Non-halogenated solvent-processed organic solar cells with approaching 20% efficiency and improved photostability. *Angew. Chem. Int. Ed.* **63**, e202404297 (2024).
27. Fan, H. et al. Phenanthrene treatment for O-xylene-processed PM6:Y6-based organic solar cells enables over 19% efficiency. *Adv. Energy Mater.* **64**, 2405257 (2024).
28. Han, C. et al. A halogen-free and universally volatile solid additive enables binary organic solar cells to exceed 19% efficiency. *Adv. Funct. Mater.* **35**, 2416381 (2024).
29. Zhang, R. et al. Equally high efficiencies of organic solar cells processed from different solvents reveal key factors for morphology control. *Nat. Energy* **10**, 124–134 (2025).
30. Guo, C. et al. Light-induced quinone conformation of polymer donors toward 19.9% efficiency organic solar cells. *Energy Environ. Sci.* **17**, 2492–2499 (2024).
31. Cui, F. et al. Using an external electric field to tune active layer morphology enabling high-efficiency organic solar cells via ambient blade coating. *Sci. Adv.* **10**, ead05460 (2024).
32. Wang, W. et al. H-bonded organic frameworks as ultrasound-programmable delivery platform. *Nature* **638**, 401–410 (2025).
33. Guo, G. et al. Enhanced porosity and permeability of three-dimensional alginate scaffolds via acoustic microstreaming induced by low-intensity pulsed ultrasound. *Ultrason. Sonochem.* **37**, 279–285 (2017).
34. Sun, M. et al. Overcoming disordered preaggregation in liquid state for highly efficient organic solar cells printed from nonhalogenated solvents. *Adv. Energy Mater.* **13**, 2203465 (2023).

35. Ashokkumar, M. et al. The characterization of acoustic cavitation bubbles – an overview. *Ultrason. Sonochem.* **18**, 864–872 (2011).
36. Brotchie, A. et al. Effect of power and frequency on bubble-size distributions in acoustic cavitation. *Phys. Rev. Lett.* **102**, 084302 (2009).
37. Wang, C. et al. Sonochemistry: Materials science and engineering applications. *Coord. Chem. Rev.* **526**, 216373 (2025).
38. Liang, H. et al. A rare case of brominated small molecule acceptors for high-efficiency organic solar cells. *Nat. Commun.* **14**, 4707 (2023).
39. Su, W. et al. Solitons in polyacetylene. *Phys. Rev. Lett.* **42**, 1698–1701 (1979).
40. Zhao, Q. et al. Balancing the H- and J-aggregation in DTS(PTTh₂)₂/PC₇₀BM to yield a high photovoltaic efficiency. *J. Mater. Chem. C*, **3**, 8183–8192 (2015).
41. Wang, Q. et al. Acoustic radiation force on small spheres due to transient acoustic fields. *Phys. Rev. Appl.* **15**, 044034 (2021).
42. Ji, Y. et al. Synergistic effect of incorporating intra- and intermolecular charge transfer in nonfullerene acceptor molecules for highly-efficient organic solar cells. *J. Mater. Chem. A* **9**, 16834–16840 (2021).
43. Clark, J. et al. Role of intermolecular coupling in the photophysics of disordered organic semiconductors: aggregate emission in regioregular polythiophene. *Phys. Rev. Lett.* **98**, 206406 (2007).
44. Zhao, Q. et al. H- and J-aggregation inspiring efficient solar conversion. *J. Mater. Chem. A* **9**, 1119–1126 (2021).
45. Zhang, G. et al. Delocalization of exciton and electron wavefunction in non-fullerene acceptor molecules enables efficient organic solar cells. *Nat. Commun.* **11**, 3943 (2020).
46. Qiao, J. et al. Enhanced exciton delocalization in organic near-infrared photodetectors via solid additive-mediated J-aggregation. *Adv. Mater.* **37**, 2418844 (2024).
47. Wang, J. et al. Two well-compatible acceptors with efficient energy transfer enable ternary organic photovoltaics exhibiting a 13.36% efficiency. *Small* **15**, 1902602 (2019).
48. Chen, H. et al. A guest-assisted molecular-organization approach for >17% efficiency organic solar cells using environmentally friendly solvents. *Nat. Energy* **6**, 1045–1053 (2021).
49. Zhou, M. et al. 19.10% efficiency and 80.5% fill factor layer-by-layer organic solar cells realized by 4-bis(2-thienyl)pyrrole-2,5-dione based polymer additives for inducing vertical segregation morphology. *Adv. Mater.* **35**, 2208279 (2023).
50. Zhu, L. et al. Single-junction organic solar cells with over 19% efficiency enabled by a refined double-fibril network morphology. *Nat. Mater.* **21**, 656–663 (2022).
51. Cai, Y. et al. Vertically optimized phase separation with improved exciton diffusion enables efficient organic solar cells with thick active layers. *Nat. Commun.* **13**, 2369 (2022).
52. Cai, Y. et al. A well-mixed phase formed by two compatible non-fullerene acceptors enables ternary organic solar cells with efficiency over 18.6%. *Adv. Mater.* **33**, 2101733 (2021).
53. Cui, F. et al. Vertical-phase-locking effect in efficient and stable all-polymer-hosted solar cells. *ACS Energy Lett.* **7**, 3709–3717 (2022).
54. Chen, Z. et al. Trap state induced recombination effects on indoor organic photovoltaic cells. *ACS Energy Lett.* **6**, 3203–3211 (2021).
55. Wang, R. et al. Charge separation from an intra-moiety intermediate state in the high-performance PM6:Y6 organic photovoltaic blend. *J. Am. Chem. Soc.* **142**, 12751–12759 (2020).
56. Jiang, K. et al. Suppressed recombination loss in organic photovoltaics adopting a planar-mixed heterojunction architecture. *Nat. Energy* **7**, 1076–1086 (2022).
57. Xu, R. et al. Enhancing singlet excitons delocalization via selective asymmetric fluorination of electron acceptors for efficient organic solar cells. *Sci. Adv.* **11**, eadt6024 (2025).
58. Chen, X. et al. A unified description of non-radiative voltage losses in organic solar cells. *Nat. Energy* **6**, 799–806 (2021).
59. Zhang, K. et al. Donor-acceptor interfacial dipole polarization for efficient and stable thick-film organic photovoltaics. *Nano Energy* **134**, 110546 (2025).
60. Guha, S. et al. Temperature-dependent photoluminescence of organic semiconductors with varying backbone conformation. *Phys. Rev. B* **67**, 125204 (2003).
61. Guo, Q. et al. Enhancing the performance of organic solar cells by prolonging the lifetime of photogenerated excitons. *Adv. Mater.* **32**, 2003164 (2020).
62. Li, Q. et al. A conical intersection model to explain aggregation induced emission in diphenyl dibenzofulvene. *Chem. Commun.* **49**, 5966–5968 (2013).
63. Gao, Y. et al. Excited-state decay paths in tetraphenylethene derivatives. *J. Phys. Chem. A* **121**, 2572–2579 (2017).
64. Ma, R. et al. Revealing the underlying solvent effect on film morphology in high-efficiency organic solar cells through combined ex situ and in situ observations. *Energy Environ. Sci.* **16**, 2316–2326 (2023).
65. Zhang, L. et al. Improving efficiency and flexibility of non-halogenated solvent-processed dual-layer organic solar cells through solvent vapor annealing. *Org. Electron.* **130**, 107075 (2024).
66. Hughes, M. et al. Determining the dielectric constants of organic photovoltaic materials using impedance spectroscopy. *Adv. Funct. Mater.* **28**, 1801542 (2018).
67. Huang, J. et al. Polymer bulk heterojunction solar cells employing Förster resonance energy transfer. *Nat. Photonics* **7**, 479–485 (2013).
68. Honda, S. et al. Selective dye loading at the heterojunction in polymer/fullerene solar cells. *Adv. Energy Mater.* **1**, 588–598 (2011).
69. Wang, J. et al. Increasing donor-acceptor spacing for reduced voltage loss in organic solar cells. *Nat. Commun.* **12**, 6679 (2021).
70. Du, X. et al. Unraveling the microstructure-related device stability for polymer solar cells based on nonfullerene small-molecular acceptors. *Adv. Mater.* **32**, 1908305 (2020).
71. An, K. et al. Mastering morphology of non-fullerene acceptors towards long-term stable organic solar cells. *Nat. Commun.* **14**, 2688 (2023).
72. Qin, Y. et al. The performance-stability conundrum of BTP-based organic solar cells. *Joule* **5**, 2129–2147 (2021).

Acknowledgements

This work was supported by the National Natural Science Foundation of China (52320105003, 52203333). X.T.H acknowledges support from the Taishan Scholars Program (tstp20230610). K.N.Z acknowledges support from the Shandong Provincial Natural Science Foundation (ZR2024QA063) and the Young Scholars Program of Shandong University, China. T.W acknowledges support from the National Natural Science Foundation of China (22309034). Y.W acknowledges support from the National Natural Science Foundation of China (32402291). The authors would like to thank the Analytical Center for Structural Constituent and Physical Property of Core Facilities Sharing Platform, Shandong University for use of the femtosecond TA spectroscopy system (TAS, 2104573S), and the Instrument Improvement Funds of Shandong University Public Technology Platform (ts20230101). The authors are grateful to the Shanghai Synchrotron Radiation Facility (beamline BL16B1) for support with GIXS measurements.

Author contributions

X.H. developed the concept and conceived the idea. M.Z. and K.Z. performed the optical and electrical characterization, conducted the device fabrication, device measurements, and data collection, wrote the original draft. X.X., C.H., K.Z., and T.S. optimized the global fitting model

of TA spectra, tested the TRIR data and conducted relative analysis. D.W. and K.G. conducted the tight-binding model combined with a non-adiabatic evolution calculation and analyzed the calculated results. J.S. and Y.S. conducted the certification of the performance of OSCs from the National Institute of Metrology, China. R.Z. and J.C. assisted with experimental testing. Y.W. and M.A. assisted with data analysis. T.W. and Z.W. conducted the flexible device fabrication using the roll-to-roll technique. J.Q., H.Y., X.D., W.Q., and F.C. contributed to revisions of the manuscript. X.H. directed and supervised the whole project. All the authors participated in the data analysis and commented on the manuscript.

Competing interests

The authors declare no competing interests.

Additional information

Supplementary information The online version contains supplementary material available at <https://doi.org/10.1038/s41467-025-65447-y>.

Correspondence and requests for materials should be addressed to Kangning Zhang, Yanming Sun or Xiaotao Hao.

Peer review information *Nature Communications* thanks Nicola Gasparini, and the other, anonymous, reviewer(s) for their contribution to the peer review of this work. A peer review file is available.

Reprints and permissions information is available at <http://www.nature.com/reprints>

Publisher's note Springer Nature remains neutral with regard to jurisdictional claims in published maps and institutional affiliations.

Open Access This article is licensed under a Creative Commons Attribution-NonCommercial-NoDerivatives 4.0 International License, which permits any non-commercial use, sharing, distribution and reproduction in any medium or format, as long as you give appropriate credit to the original author(s) and the source, provide a link to the Creative Commons licence, and indicate if you modified the licensed material. You do not have permission under this licence to share adapted material derived from this article or parts of it. The images or other third party material in this article are included in the article's Creative Commons licence, unless indicated otherwise in a credit line to the material. If material is not included in the article's Creative Commons licence and your intended use is not permitted by statutory regulation or exceeds the permitted use, you will need to obtain permission directly from the copyright holder. To view a copy of this licence, visit <http://creativecommons.org/licenses/by-nc-nd/4.0/>.

© The Author(s) 2025